The decoupling and synergy strategy to construct multiscales from nano to millimeter for heat pipe

Xianbing Ji [a], Jinliang Xu [a,*], Hongchuan Li [a], Yanping Huang [b]

[a] The Beijing Key Laboratory of Multiphase Flow and Heat Transfer, North China Electric Power University, Beijing 102206, PR China
[b] CNNC Key Laboratory on Nuclear Reactor Thermal Hydraulics Technology, Nuclear Power Institute of China, Chengdu 610041, PR China

ARTICLE INFO

ABSTRACT

We decouple a heat pipe into capillary pressure, flow resistance, condensation heat transfer, and assign specific length scale to adapt each function. We verify the synergy of various length scales to activate various functions. The strategy guides multiscale design to realize an enhancement of capillary pressure, a well management of flow resistance and an ultra-thin liquid thickness on condenser surface. The porous wick consists of a particle sub-layer and 3D mastoid process array. The tips of mastoid process directly contact the condenser wall. Four vapor chambers are formed by sintering d_m = 73.8 μm without oxidation (#1), with oxidation (#2), d_m = 556 nm without oxidation (#3) and with oxidation (#4), respectively. Liquid suction and heat transfer experiments were performed. Four types of evaporator temperatures versus inclination angles were observed. Small difference is found between bottom and top heating modes. The multiscale wick influences the vapor–liquid phase distribution to cause the difference between side and other heating modes. The d_m = 73.8 μm particle sintering with nano-roughness successfully balance various conflicts among capillary pressure, vapor–liquid interface area, flow resistance and liquid removal from the condenser surface. Nano-roughness increases the vapor–liquid interface area to have 3–4 times of evaporation heat transfer coefficients compared with smooth particle surface. Nano-roughness increases the wettability to capture liquid from condenser, having ~18 times of condensation heat transfer coefficients to those without nano-roughness. The d_m = 556 nm particle sintering and nano-roughness are the poor match for heat pipes. This paper gives a clue to construct multiscale wicks for heat pipes and ensures better performance at varied gravity such as micro-gravity environment.

© 2015 Elsevier Ltd. All rights reserved.

1. Introduction

Heat pipes have been widely used from the invention on 1950s. Various miniature heat pipes, such as micro heat pipes [1,2], loop heat pipes [3,4], pulsating heat pipes [5,6] and vapor chambers [7,8], have received great attention in recent 20 years. Besides, the fast developing space technologies need high performance heat pipes for electronics cooling, or for other applications, under varied gravity force levels [9]. A perfect heat pipe shall have the following characteristics: (1) heat pipe shall start up without apparent temperature excursion to avoid the start up burn-out; (2) heat pipe shall maintain high heat transfer coefficients during normal operation; (3) the operation of heat pipe shall be stable; (3) heat pipe shall have high critical heat fluxes to avoid dry-out.

Heat pipes are phase change devices with capillary force due to the wall wicking. However, gravity force still plays important role. Most of heat pipes are working as thermosiphon, that is, the con-

denser part is above the evaporator part. Heat pipes have poorer performance at horizontal position [10]. Under earth gravity, it is difficult to maintain good performance when the evaporator part is above the condenser part [11]. This is because liquid shall be recycled to evaporator by capillary force against gravity. The space technology needs heat pipes to be working under varied gravities. For example, on the moon, the gravity is only about 1/6 of that on the earth [12]. Heat pipes on board a space ship shall work under micro or zero gravities [13].

Heat pipe operation at varied gravities is dependent on vapor–liquid phase distribution inside. The widely used porous media with a single length scale is difficult to regulate the phase distribution under varied gravities. There are many conflicts if one relies on a single length scale for the wick structure. These conflicts are summarized as follows.

1.1. Conflict between capillary pressure and viscous force

A key challenge for implementing thin film evaporation is the ability to efficiently deliver liquid to the heater surface. Recent

---

* Corresponding author. Tel./fax: +86 10 61772613.
  E-mail address: xjl@ncepu.edu.cn (J. Xu).

Nomenclature

A	surface area, m^2
A_{heater}	snake heater area, m^2
a	nanowires diameter, m
Bo	Bond number
b	minimum distance between two neighboring nano-wires, m
D	vapor chamber diameter, m
d	particle diameter, m
d_1	smaller pore diameter, m
d_2	larger pore diameter, m
dE	surface energy difference between state A and state B, W
dK	work needed for the bubble traveling from state A to state B, W
dS_1	bubble traveling distance in smaller pore, m
dS_2	bubble traveling distance in larger pore, m
d_m	mean particle diameter, m
d_p	single length scale, m
g	gravity, m/s^2
H	nanowires height, m
h	heat transfer coefficient, W/m^2 K
L	characteristic length, m
l	capillary length, m
N	particle number
P_1	pressures in smaller pore, Pa
P_2	pressures in larger pore, Pa
Q	heating power, W
q	heat flux, W/m^2
R	thermal resistance, K/W
r	roughness factor
r_b	bottom part radius of vapor chamber, m
r_t	top part radius of vapor chamber, m

T	temperature, °C
T_θ	evaporator center temperature at θ

Greek symbols

α	contact angle between liquid and solid surface, °
α_w	contact angle between liquid and microstructure, °
β	non-dimensional parameters, $\beta = b/a$
Δ	distance away from the heater, m
δ	liquid layer thickness, m
δ_s	liquid layer thickness within the porous stacks, m
ε	deviation degree factor
θ	inclination angles
ρ	density, kg/m^3
σ	surface tension force, N/m
ξ	non-dimensional parameters, $\xi = H/a$

Subscript

c	condenser
c, c	condenser center
ave	average
e	evaporator
e, c	evaporator center
$e, 1 \sim e, 8$	location on evaporator wall
$c, 1 \sim c, 8$	location on condenser wall
g	gas
i	ith particle
l	liquid
$loss$	heat loss
s	solid
w	wall
v	vapor

efforts have investigated super-hydrophilic micro/nano structured surfaces, such as micro-pillar arrays, sintered copper powders, and carbon nanotubes, to transport liquid *via* capillarity [14–16]. However, capillary pressure and viscous resistance are coupled with each other. By reducing the characteristic structure size, the capillary pressure increases, but liquid transport is inhibited due to the significant viscous resistance associated with the small spacing.

1.2. Conflict between capillary pressure and vapor venting

Considering boiling/evaporation in a wick structure with a single length scale d_p, capillary pressure is increased if d_p decreases. Meanwhile, the volume will be expanded by ~100–1000 times if liquid is changed to vapor. The smaller pore size definitely blocks the vapor venting and hinders the liquid toward the heater surface to induce critical heat flux (CHF) [17,18]. Alternatively, larger pores are helpful for vapor venting but are not useful to generate sufficient capillary pressure for liquid supply [19,20]. The two and three dimensional (2D/3D) modulated porous wicks [21,22], and the biporous wicks [23,24], are able to overcome the conflict between capillary pressure and vapor release. Ji et al. [25] found that the 3D modulated porous wicks significantly increase critical heat fluxes, which are 3.7 times of that on plain smooth surface. Semenic and Catton [26] used a wick consisting of large clusters of small copper particles and suggested that small pores serve to transport liquid to the boiling sections by capillary suction, while large pores between the clusters facilitate vapor transport away from the wick thus enhancing the overall heat transfer performance. Ćoso et al. [27] showed both enhancements of boiling/evaporation heat transfer

coefficients and critical heat fluxes by using biporous wick with the silicon fabrication technique.

1.3. Balance between heat transfer coefficients and critical heat fluxes

For an efficient boiling/evaporation surface, one shall balance heat transfer coefficients and critical heat fluxes. Recently, micro/-nano structured surfaces have been investigated widely [28,29]. The textured surfaces strongly influence the surface wettability. A hydrophobic surface maintains high evaporation heat transfer coefficients due to thin liquid film on the surface, but the operation range of heat fluxes is narrowed due to weak ability to suck liquid toward the heater surface [30]. On the contrary, a hydrophilic surface expands the heat flux operation range but heat transfer coefficients are not large. The problem is how to construct a surface that not only maintains high heat transfer coefficients but also has high critical heat fluxes?

1.4. Coupling of the evaporator and condenser

The vapor–liquid two-phases are recycled between evaporator and condenser. Heat pipe performance is relied on the coupling between evaporator and condenser. For a heat spreader, liquids on the condenser surface should be removed successfully to maintain better condenser performance. The evaporator shall receive liquid from the condenser surface. For a conventional vapor chamber, the condensed liquid travels a distance of D and returns to the evaporator, where D is the vapor chamber diameter. This increases the liquid film thickness to deteriorate the condenser performance

[31]. Boreyko and Chen [32] proposed self-propelled jumping drops on a super-hydrophobic condenser surface, offering a new mechanism to return the working fluid to the evaporator.

In summary, there are many conflicts if one uses porous media with a single pore scale in a heat pipe. Various phenomena and factors are coupled with each other. The varied gravity level makes the problem more complicated. The multiscale is a possible solution to overcome the conflicts. In this paper, the *decoupling and synergy* strategy is proposed for multiscale construction. A perfect vapor chamber constructs multiscales by (1) *Decoupling*: a heat pipe is decoupled into various functions of capillary pressure generation, vapor–liquid interface area, liquid and vapor transport and condensation heat transfer. Because different functions require different pore length scales to adapt, assign a suitable length scale to activate specific functions. Do not let a single length scale do everything. (2) *Synergy*: by experimental and theoretical analysis, one identifies how to synergy different length scales to achieve a comprehensive and better heat pipe performance.

Here, vapor chambers were fabricated by sintering d_m = 73.8 μm or d_m = 556 nm copper powders on evaporator walls. The porous wick consists of a particle sub-layer close to the evaporator wall and 3D mastoid process array. The tips of porous stacks directly contact condenser. The vapor chambers include fruitful length scales. Copper particles are soldered to form a pore with ∼$0.21d_m$ scale. Parallel particle chains form pore channel with width of ∼d_m and length longer than d_m. Small pores (∼$0.21d_m$) create sufficient capillary force, while pore channels (∼d_m scale) transport liquid and vapor. Thermal oxidation generates nano-roughness on particle surfaces to increase surface area and wettability. Experiments were performed with and without nano-roughness. The results showed that the d_m = 73.8 μm particle sintering with nano-roughness reflects the "best" match of various

length scales to activate different functions. The nano-roughness not only significantly increases vapor–liquid interface area to enhance the evaporation heat transfer, but also increases wettability for liquid collection from the condenser surface to maintain high condensation heat transfer coefficients. However, the d_m = 556 nm particle sintering with and without nano-roughness involves larger viscous resistance for fluid transport, indicating poorer match of different length scales.

2. Experimental setup and facility

2.1. Vapor chamber assembly

Fig. 1a shows the vapor chamber assembly. A fin heat sink and a thin film heater were above and below the vapor chamber, respectively. A 5 V DC driven fan was positioned at the top of the fin heat sink to dissipate heat to environment. The fin heat sink had exactly the same diameter as that of the vapor chamber. There are totally 23 fins, each having a thickness of 2.0 mm and a height of 53 mm. The gap between two neighboring fins is 2.5 mm. The glue was filled between the heat sink and the vapor chamber, and between the vapor chamber and the thin film heater. Thus, the contact thermal resistances at the two junction surfaces were apparently reduced.

Fig. 1b shows the thin film heater at the back vapor chamber surface. The heater had snake shape, which can sustain 45 V DC voltage with its resistance of 14 Ω. The effective heating area was 1.4 cm² (red part of the snake heater). The maximum heating power was about 200 W. The heater was driven by a power supply system, consisting of a voltage stabilizer, a voltage transformer and a power-meter. The voltage stabilizer minimized the voltage oscillation versus time. By adjusting the voltage transformer, one can
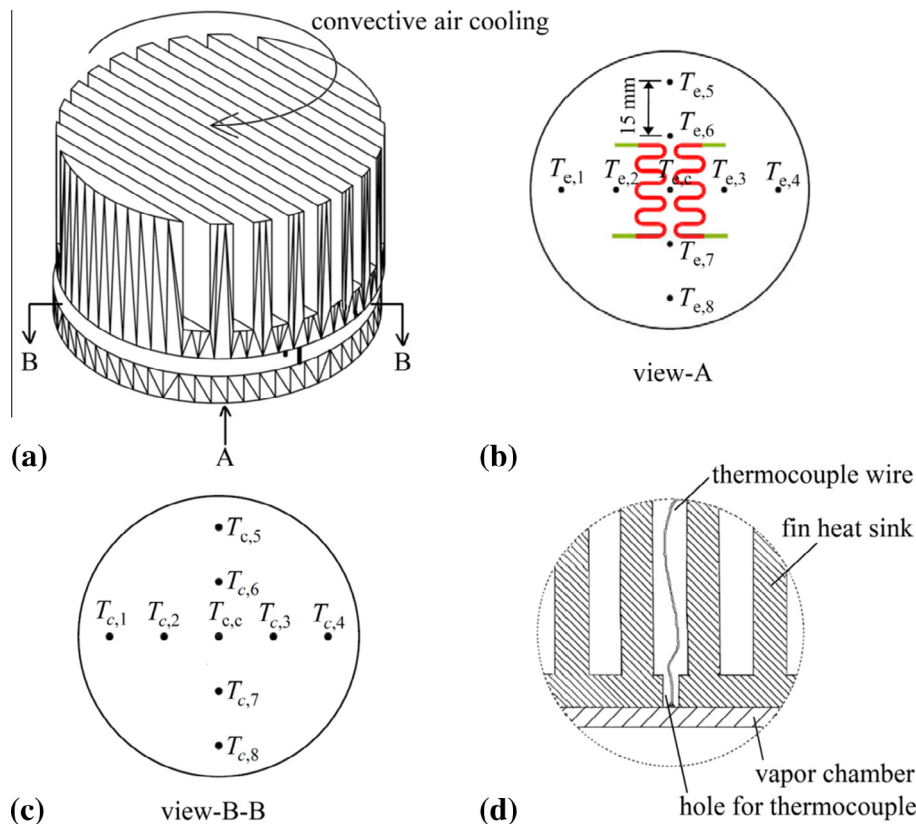

Fig. 1. The vapor chamber (a: vapor chamber assembly, b: heater and thermocouples on the vapor chamber bottom surface, c: thermocouples on the condenser surface, d: thermocouple wires penetrating from the fin heat sink).

obtain a stable voltage output to yield an adjustable heating power to the snake heater.

Nine thermocouple wires ($T_{e,1-Te,8}$) were welded on the evaporator surface, with the subscript e meaning the evaporator. The thermocouple $T_{e,c}$ was at the evaporator center. The distance between two neighboring thermocouples was 15 mm. Nine thermocouples were welded on the top vapor chamber surface (see Fig. 1c), with the subscript c meaning the condenser. Fig. 1d shows the arrangement of condenser thermocouples and the fin heat sink. There are miniature holes on the base substrate of the fin heat sink to penetrate thermocouple wires out of the fin heat sink. There was a thermocouple inside the vapor chamber to measure the vapor temperature T_v (not shown in Fig. 1).

Before welding the vapor chamber, all the pieces were rinsed by methanol solution followed by drying. The vacuum and charging procedures were performed using a special facility fabricated in our laboratory. The vacuum pressure could be 0.06 Pa using the molecular pump. The vapor chamber was filled with the deionized water and sealed. The net liquid charged in the vapor chamber was the weight difference before and after the vapor chamber was charged with liquid. The weight measurement was performed by an electronic balance with an uncertainty of 0.01 g. The inside volume of the vapor chamber is defined as that was not occupied by metal and metallic particles. The measured volume was 11.5 ml. The final charged water was 2.3 ml. Thus, the liquid charge ratio was about 20%. Complete wetting the porous structures (including the porous sub-layer and mastoid processes) needs about 15% liquid charge ratio. Hence, the 20% liquid charge ratio indicates about 5% extra liquid outside of the porous structure. The vapor chamber assembly was positioned on a rotating facility with the inclination angle uncertainty of 0.5°. The heating power and the temperatures were recorded by a Hewlett–Packard data acquisition system.

2.2. Vapor chamber

Fig. 2a shows the *Calathea zebrina* leaf to have relatively uniform mastoid process. A water droplet spreads rapidly and completely wets the surface in a few seconds. On the leaves of *Ruellia devosiana*, 5 μL water was found to require 0.2 s only to completely spread [33,34]. Fig. 2b shows the mastoid processes sintered on the evaporator surface of the vapor chamber, noting the A–A cross section was shown. The porous structure is super-hydrophilic. Over a 90 mm inside chamber diameter, there are 254 mastoid processes. Fig. 2b implements the decoupling strategy to construct multiscale structure for vapor chambers.
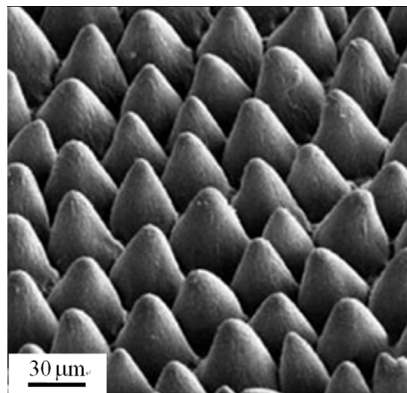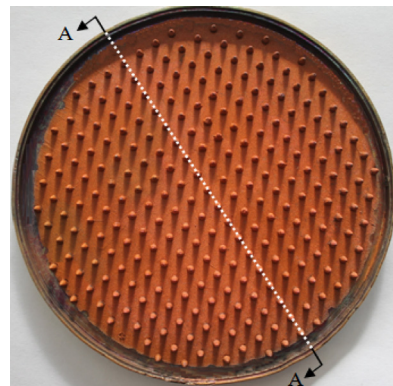
2.2.1. Overcome the conflict between capillary pressure and viscous force

Porous media within the mastoid process contains pores with scale of $\sim 0.21 d_m$, which creates sufficient capillary pressure. Parallel particle chains form pore channel with width of d_m scale and length longer than d_m, acting for the liquid transport channel.

2.2.2. Overcome the conflict between capillary pressure and vapor venting

Pores in $\sim d_m$ scale within mastoid process generates capillary pressure. Phase change heat transfer from liquid to vapor involves large volume expansion. Thus, the vacuum volume not occupied by the mastoid processes is for vapor expansion. The 3D porous stacks in vapor chambers overcome the conflict between capillary pressure and vapor venting.

2.2.3. Coupling between evaporation heat transfer and condensation heat transfer

The multiscale wicks are expected to enhance the evaporation heat transfer. The porous media is hydrophilic. The nanoroughness on particle surface enhances the wettability, which is expected to remove liquid from the condenser surface. In other word, the 3D mastoid process array successfully couples the evaporation and condensation heat transfer.

To overcome the above conflicts, the hybrid micro/nano wick is paid attention. Section 3 discusses the synergy to see if these length scales are adapted with each other to have better heat pipe performance. Fig. 3 shows the vapor chamber for anti-gravity operation, where T_v represents the vapor temperature in the vapor chamber. The heater was positioned at the evaporator center. The chamber had a 90 mm diameter and a 2.5 mm inner height. The evaporator wall had a particle sub-layer with a 0.5 mm thickness. Each mastoid process had a 1.5 mm base diameter and a 2.0 mm height. The distance between the two neighboring mastoid processes was 5.5 mm. The tips of mastoid processes directly contact the condenser surface, passively collecting liquid from the condenser surface towards the porous stacks. The design prevents the evaporator from dry-out and ensures ultra-thin liquid film on the condenser. The multiscale wick structure balances the conflicts among the capillary pressure, flow resistance and condensation heat transfer.

High quality copper powders were used for sintering. The d_m = 73.8 μm particles were selected by screen mesh. The selection process was repeated by two times, one with a larger screen mesh and the other with a smaller screen mesh. In such a way, the particles had a narrow size range. Two characteristic sizes of
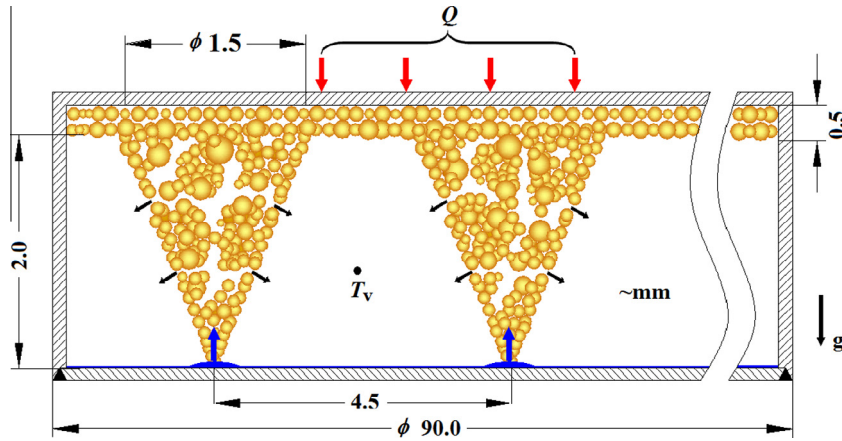

(a) The uniform conical structures on a leaf of

Calathea zebrine [38]

(b) The evaporator photo for vapor chamber

Fig. 2. The 3D mastoid process in nature (a) and sintered evaporator for vapor chamber (b).

Fig. 3. The vapor chamber dimensions (dimensions are in mm).

d_m = 73.8 μm and d_m = 556 nm were used, where d_m is the mean particle diameter. The SEM (scanning electron microscope) photos were taken to perform the statistical analysis, yielding d_m as

$$N \times \frac{\pi}{6} d_m^3 = \sum_{i=1}^{N} \frac{\pi}{6} d_i^3 \tag{1}$$

where N is the particle number involved in the statistical analysis, and d_i is the ith particle diameter.

A 0.5 mm particle layer was sintered on the evaporator wall. A graphite mold with conical cavities was fabricated, cleaned and dried. The cavity size was exactly identical to the mastoid process. The cavities of the graphite mold were filled with copper particles. Bonding the evaporator and the graphite mold tightly forms an assembly. The assembly was in an oven for sintering with vacuumed air to prevent the particle oxidation. The sintering was performed in a nitrogen–hydrogen gas protection environment, further preventing the particle oxidation. The sintering temperature was dependent on the particle size. For the 73.8 μm particle sintering, the sintering temperature was 900 °C and the sintering time was 3.5 h. Alternatively, for the 556 nm particle sintering, the sintering temperature was 650 °C, lasting 3 h. After the sintering, the sample was kept in the oven, until its temperature was decreased to a value slightly higher than the environment. Then the sample was taken out of the oven for further process.

Four evaporator samples were prepared. The #1 and #3 samples are with d_m = 73.8 μm and d_m = 556 nm particles, respectively. Both are without thermal oxidation. The #2 and #4 samples are with d_m = 73.8 μm and d_m = 556 nm particles, respectively. But they are with thermal oxidation, which were performed in the oven for another one hour by sintering the particles in air environment.

2.3. Data reduction and uncertainty analysis

Before the formal experiment, heat loss was experimentally determined without convective air cooling. A copper plate with identical diameter and thickness of the vapor chamber was tested. The snake heater was arranged on the center surface of the copper plate. The copper plate was wrapped by high quality thermal insulation material. The heating power was recorded when the center wall temperatures are reached specific values such as 40–120 °C. The temperature range is the same as the operation range of the four vapor chambers. Thus, a specific wall temperature corresponds to a specific heat loss.

For the vapor chamber experiment, the heat flux on the evaporator wall was

$$q = \frac{Q - Q_{loss}}{A_{heater}} \tag{2}$$

where Q is the heating power from the power-meter, Q_{loss} is the heat loss at the corresponding wall temperature $T_{e,c}$, A_{heater} is the snake heater area, which is 1.4 cm^2 (see the red part of Fig. 1b). The evaporator thermal resistance is

$$R_e = \frac{(T_{e,c} - T_v)}{Q - Q_{loss}} \tag{3}$$

where $T_{e,c}$ is the wall temperature at the evaporator center (see Fig. 1b). The evaporator heat transfer coefficient is

$$h_e = \frac{Q - Q_{loss}}{A_{heater}(T_{e,c} - T_v)} \tag{4}$$

The condenser thermal resistance is

$$R_c = \frac{(T_v - T_{c,ave})}{Q - Q_{loss}} \tag{5}$$

where $T_{c,ave}$ is the average temperature on the top condenser surface (see Fig. 1c), which is

$$T_{c,ave} = \frac{1}{9} \left[T_{c,c} + \sum_{i=1}^{8} T_{c,i} \right] \tag{6}$$

The condensation heat transfer coefficient is

$$h_c = \frac{Q - Q_{loss}}{A_c(T_v - T_{c,ave})} \tag{7}$$

where A_c is the condenser wall area having a 90 mm diameter. The power measurement had the uncertainty of 0.1 W. The temperature measurement had the uncertainty of 0.2 °C. The standard error propagation theory [35] yields the uncertainty of 4.9% for evaporator heat transfer coefficients, and 6.3% for condensation heat transfer coefficients.

3. Results and discussion

3.1. SEM pictures

Fig. 4a–c shows the #1 (73.8 μm without oxidation) sintering particles. The pore network is easily seen. Particles are clearly seen to be soldered by sintering (see Fig. 4c). The welding points apparently reduce the contact thermal resistance between neighboring particles. The pore size is about 21% of the particle diameter [36], which is ∼15 μm for the #1 particle sintering. However, not all the neighboring particles can be soldered together. Two parallel
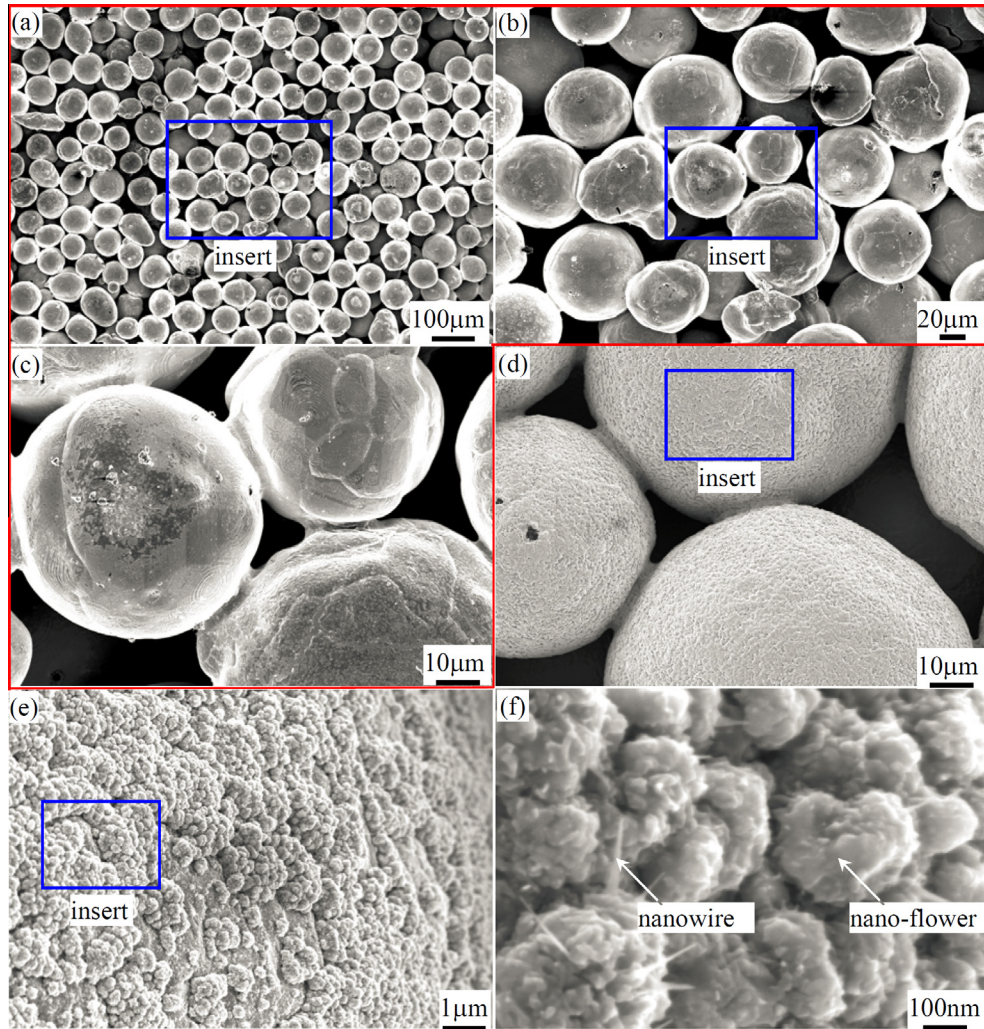
Fig. 4. SEM images (a, b and c are for #1 particle sintering, d, e and f are for #2 particle sintering).

particle chains are found to create a pore channel, having its width in particle diameter scale. The pore channel length is longer than the particle size. The #1 vapor chamber had three length scales: (1) pores in $\sim$15 μm scale; (2) pore channels with width of $\sim d_m$ = 73.8 μm, and length longer than d_m; (3) $\sim$mm scale outside of the mastoid process. Fig. 4d–f shows the #2 particle sintering with thermal oxidation. The CuO nanostructure includes nanoflowers array and nanowires (see Fig. 4f). Nanowires are with $\sim$10 nm diameter and $\sim$100 nm length. Thus, the #2 vapor chamber had four length scales: (1) nano-roughness; (2) pores in d_m = 73.8 μm; (3) pore channel with width $\sim d_m$ and length longer than d_m; (4) $\sim$mm scale outside of the mastoid process.

Nanoparticle sintering is a difficult task because the sintering quality is sensitive to the sintering temperature and time. We carefully choose the sintering parameters to have perfect nanoparticle sintering. Fig. 5a–c shows the SEM images for the #3 particle sintering without oxidation. Three nano-particles are soldered together in Fig. 5c. The pore size is down to $\sim$100 nm for d_m = 556 nm. The parallel particle chains form pore channel to have $\sim d_m$ = 556 nm width and longer length. Fig. 5d–f shows nanostructures on particle surface for the #4 sample. Nano-flowers and nanowires are observed. Because nanoparticles are covered by nano-roughness, isolated nano-particle is difficult to be observed.

3.2. Liquid suction tests

Liquid is easily transported in porous media with the help of gravity. When heater is positioned above the condenser, heat pipe is working against gravity, which is a challenge task. Clean copper powders are hydrophilic to spread liquid in porous wicks. Liquid suction test was performed by gentle contacting a 1.5 mm diameter droplet of water with a mastoid process tip (see Fig. 6). The #3 sample (d_m = 556 nm without oxidation) was used. The droplet was quickly sucked into the porous stack in 60 ms.

Fig. 7 shows the liquid suction against gravity for the #1 sample (d_m = 73.8 μm without oxidation). The mastoid process tip was below its base substrate. A slim needle held a 1.5 mm diameter water droplet. The droplet was moving slowly to approach the mastoid process tip. The droplet enveloping and mastoid process were marked by red and blue colors, respectively. The attractive force between copper powders and water sucked the water drop against gravity. The suction time was only 34 ms.

Liquid suction is balanced by wettability, capillary force and viscous resistance in porous media. The smaller the particles, the smaller pore size is to create larger capillary force. This is usefully for liquid suction. On the other hand, the decrease of particle sizes narrows the pore channels to raise the viscous resistance. This explains why the drop suction time was 34 ms for the #1 sample

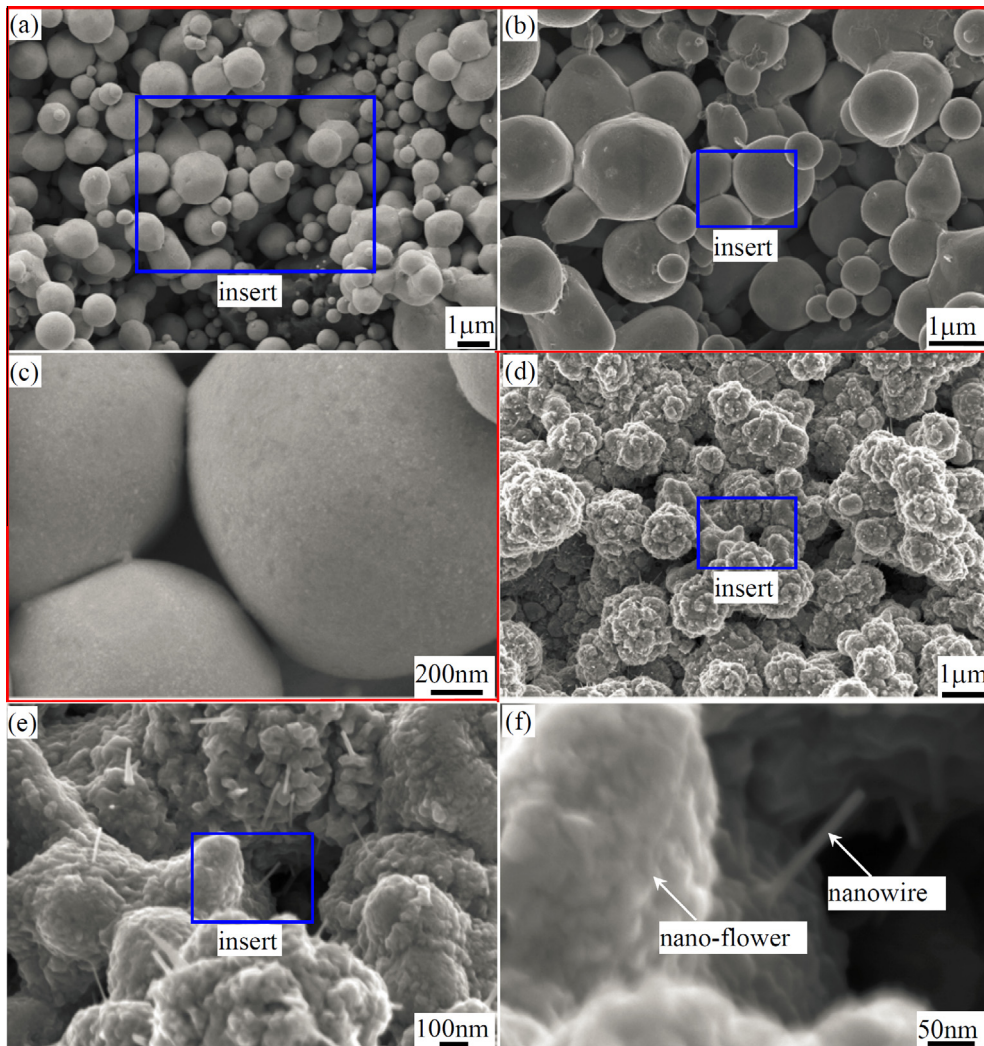**Fig. 5.** SEM images for nano particle sintering (a, b, and c are for #3 particle sintering, d, e and f are for #4 particle sintering).
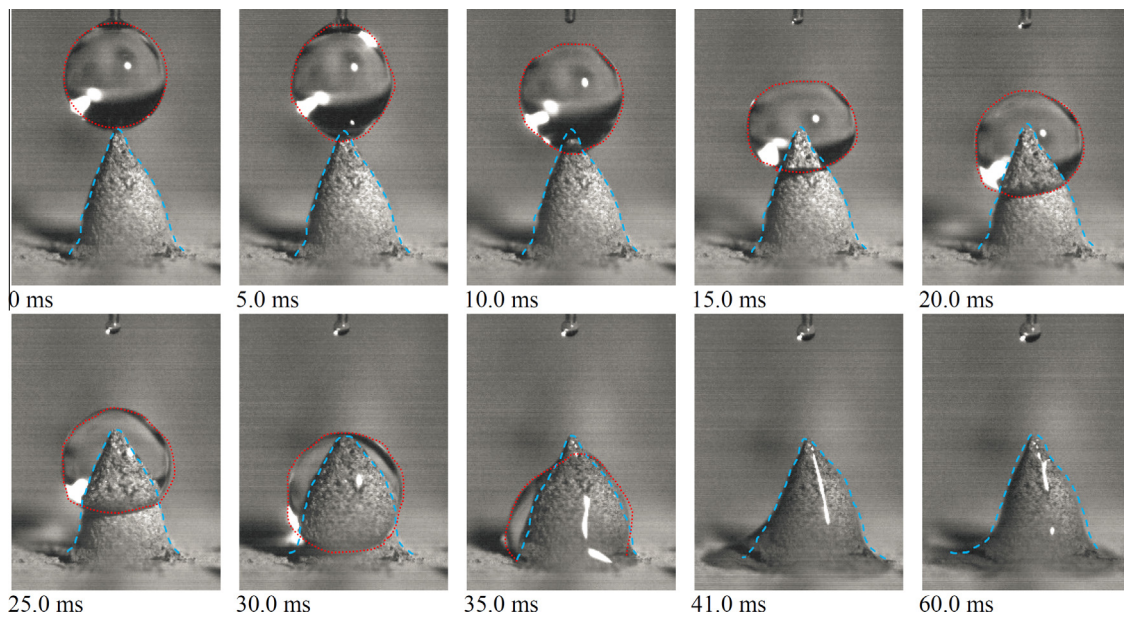

Fig. 6. The liquid suction test under gravity for #3 particle sintering (d_m = 556 nm without oxidation).
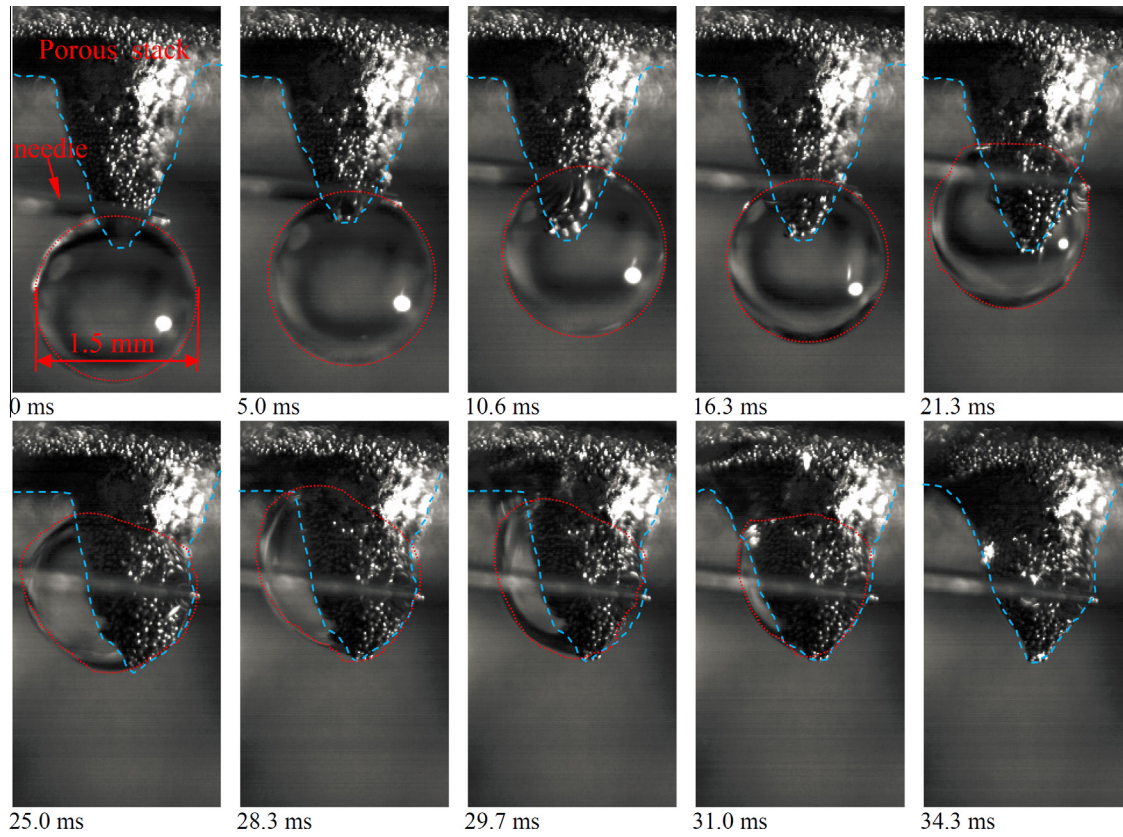
Fig. 7. The liquid suction test against gravity for #1 particle sintering (d_m = 73.8 μm without oxidation).

(d_m = 73.8 μm), which was faster than 60 ms for the #3 sample (d_m = 556 nm). Optimal particle size exists for liquid suction.

When particle size is down to micron or nano, the pore size is much smaller than the capillary length $l = (\sigma/\rho_l g)^{0.5}$, yielding negligible gravity effect on the liquid suction. This explains why hydrophilic porous stacks can suck liquid against gravity. For a hydrophilic surface, the hydrophilic degree will be enhanced if one fabricates nano-roughness on the surface [37,38]. This effect increases liquid suction capability. This is true for larger particle sintering such as d_m = 73.8 μm. For nano-particle sintering (d_m = 556 nm), the nano-roughness increases the surface wettability but the viscous resistance is sharply raised. This deteriorates the liquid suction process.

3.3. Heat pipe performance dependent on inclination angles

In order to demonstrate the effectiveness of the vapor chambers, calibration tests were performed for a copper plate and the four vapor chambers. The copper plate had identical sizes of the heat pipe samples. The fin heat sink was on the copper plate. Table 1 shows the comparison results between the copper plate and the vapor chambers. The center wall temperatures were recorded as $T_{e,c}$. The total thermal resistance was recorded as R_t. For the vapor chambers, R_t equals to $R_t = R_e + R_c$, which is deduced in Section 2.3. For the copper plate, R_t is the temperature difference of $T_{e,c}$–T_c divided by the heating power Q. Table 1 shows that the #1 vapor chamber slightly decreased $T_{e,c}$ and R_t, compared with the copper plate. The difference between the copper plate and the #2 vapor chamber is significant. For instance, the copper plate had $T_{e,c}$ = 104.7 °C and R_t = 0.392 K/W at Q = 100 W. But the #2 vapor chamber decreased $T_{e,c}$ to 69.4 °C, at which the thermal resistance is 0.1 K/W (about 1/4 of the copper plate). The #3 and #4 vapor chambers had the performance between the #1 and #2 vapor chambers. Table 1 shows the apparently improved thermal performance by the vapor chambers.

Heat transfer data was reported. Here, θ = 0°, 90° and 180° refer to the bottom, side and top heating mode, respectively. Because $T_{e,c}$ was maximum around the whole vapor chamber, $T_{e,c}$ was focused. A deviation degree factor, ε, is defined to consider the θ effect.

$$\varepsilon = \frac{T_\theta - T_{\theta=0°}}{T_{\theta=0°}} \tag{8}$$

Table 1
Calibration results among the copper plate and the four vapor chambers at the horizontal position (bottom heating mode).

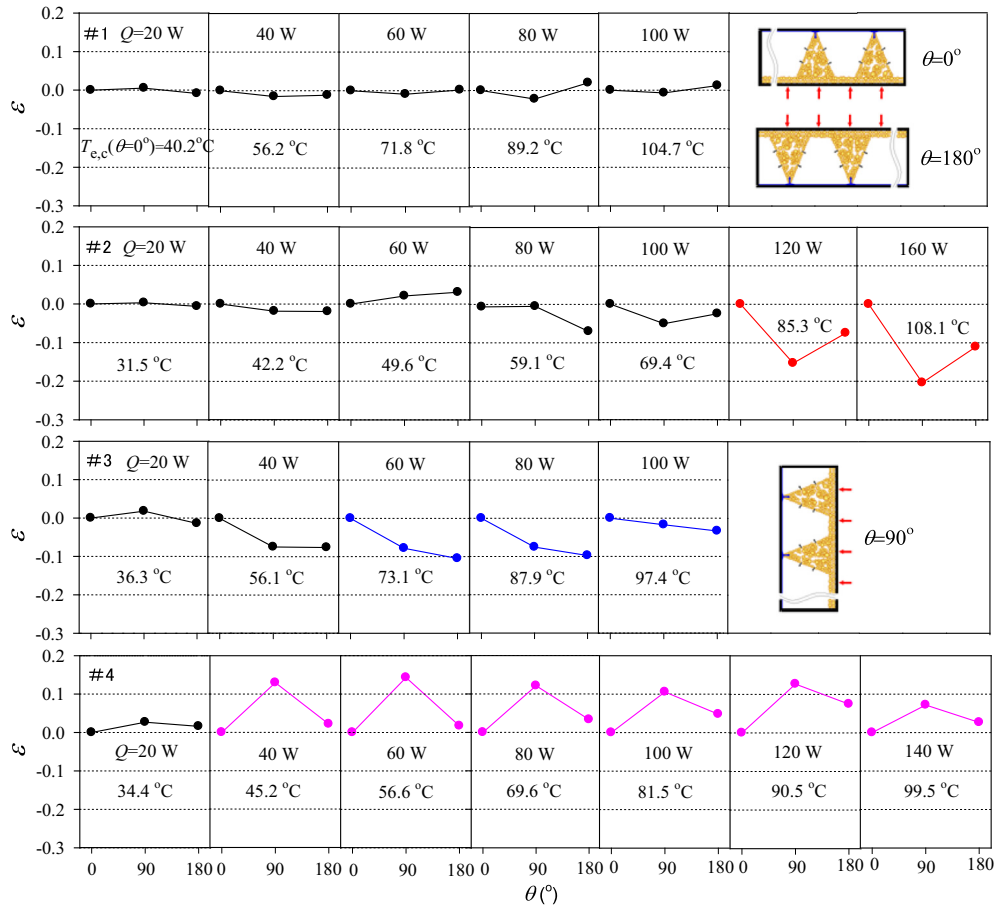| Q (W)	Copper plate		#1 vapor chamber		#2 vapor chamber		#3 vapor chamber		#4 vapor chamber	
	$T_{e,c}$ (°C)	R_t (K/W)	$T_{e,c}$ (°C)	R_t (K/W)	$T_{e,c}$ (°C)	R_t (K/W)	$T_{e,c}$ (°C)	R_t (K/W)	$T_{e,c}$ (°C)	R_t (K/W)
20	42.2	0.38	40.2	0.365	31.5	0.263	36.3	0.22	34.4	0.211
40	65.7	0.384	56.2	0.381	42.2	0.114	56.1	0.392	45.2	0.150
60	86.4	0.393	73.8	0.381	49.6	0.084	73.1	0.393	56.6	0.154
80	104.9	0.406	89.2	0.394	59.1	0.092	87.9	0.382	69.6	0.174
100	119.1	0.413	104.7	0.392	69.4	0.101	97.4	0.339	81.5	0.175

Fig. 8. The inclination angle effect on vapor chamber temperatures.

where T_θ is the evaporator center temperature at θ. Equation (8) used the temperature at bottom heating mode ($\theta = 0°$) as the reference value. The temperature unit is °C. Fig. 8 shows inclination angle patterns. Four rows correspond to the four vapor chambers. In each subfigure, $T_{\theta=0°}$ was given. The findings are as follows.

3.3.1. The vapor chamber performance

The #1 vapor chamber had the poorest performance. For instance, at $Q = 40$ W, the #1 sample had $T_{\theta=0°} = 56.2$ °C, but the #2, #3 and #4 samples had $T_{\theta=0°} = 42.2$ °C, 56.1 °C and 45.2 °C, respectively. The #2 vapor chamber had the best performance, having the lowest temperature. At $Q = 100$ W, the #2 vapor chamber had $T_{\theta=0°} = 69.4$ °C, but #1, #3 and #4 samples had $T_{\theta=0°} = 104.7$ °C, 97.4 °C and 81.5 °C, respectively. The #3 and #4 vapor chambers had the temperatures between the #1 and #2 vapor chambers. This indicates that for the #2 vapor chamber, various length scales are adapted each other to have the best performance.

3.3.2. The four types of deviation degrees

Fig. 8 shows the four types of deviation degree factors. The first type, represented by the black color, behaved uniform distribution of temperatures versus inclination angles. It happened for all the heating powers for the #1 vapor chamber. The #2, #3 and #4 vapor chambers also displayed the first type at lower heating powers. The transition powers from the first type to other type of deviation degree factors are decreased from #2 to #4 vapor chambers.

The second type of deviation degree factors, represented by the red color, occurred at larger heater powers for the #2 vapor chamber. The side heating mode ($\theta = 90°$) had lowest temperatures. The top heating mode ($\theta = 180°$) had slightly lower temperature than the bottom heating mode ($\theta = 0°$).

The third type of deviation degree factors, represented by the blue color, happened at larger heating powers for the #3 vapor chamber. The temperatures are continuously decreased from $\theta = 0°$ to 180°. The forth type of deviation degree factors, represented by the pink color, had peculiar distribution compared with the above three types of deviation degree factors. The #4 vapor chamber had higher temperatures for the side heating mode ($\theta = 90°$) than those at $\theta = 0°$ or 180°, except at $Q = 20$ W. Generally, the difference between bottom and top heating modes is small. But the side heating mode yields apparently different temperatures compared with other heating modes.

3.3.3. Explanation of the observed phenomena

Examining pore network structure in porous media (see Fig. 9a and b) explains why the #1 and #2 vapor chambers had the poorest and best performances, respectively. For the #1 sample, two length scales exist: pore size of ~ 15 μm, and pore channel with width of $\sim d_m = 73.8$ μm and length longer than d_m. Fig. 9c shows pore and pore channel, represented by d_1 and d_2, respectively. We assume a vapor bubble with one part in pore d_1 and the other part in pore channel d_2. The solid and dashed curves represent the bubble interfaces at the initial state A and the final state B, respectively. Chen et al. [39] analyzed the surface energy between state A and state B, and concluded that a pressure difference of $P_1 - P_2 = 4\sigma(1/d_1 - 1/d_2)$ drives a bubble from a smaller pore of d_1 to a larger pore of d_2, where P_1 and P_2 are the pressures in smaller pore and larger pore, respectively. For the #1 sample,
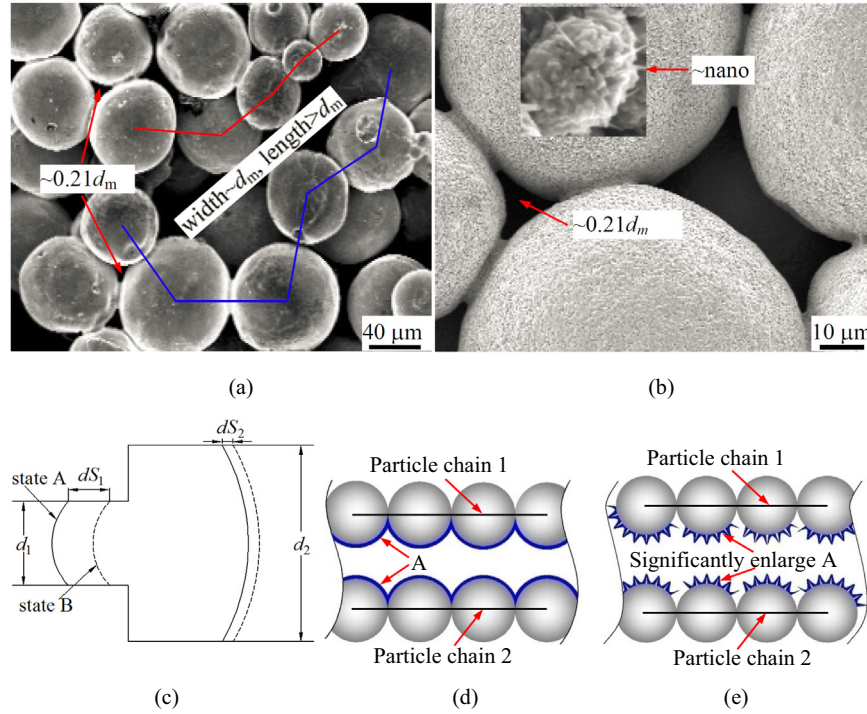
Fig. 9. Pore network for d_m = 73.8 μm particle sintering (a: without oxidation, b: with oxidation, c: surface energy analysis from smaller pore to larger pore, d: parallel particle chains formed pore channel without oxidation, e: parallel particle chains formed pore channel with oxidation).

P_1–P_2 can be up to 26.2 kPa, if one assumes d_1 = 10 μm and d_2 = 100 μm for saturation water–vapor system.

Positive P_1–P_2 yields liquid population in smaller pores and vapor population in larger pore channels. Fig. 9d and e shows pore channels for the #1 and #2 samples, respectively. The nano-roughness on particle surfaces significantly increases the liquid–vapor interface area (A). We remember that evaporation heat transfer depends on A: $Q = h_e A(T_w–T_v)$, where h_e is the evaporation heat transfer coefficient, $T_w–T_v$ is the temperature difference. The greatly increased surface area A decreases wall temperature T_w, explaining why the #2 vapor chamber had better performance than the #1 vapor chamber.

For the #3 and #4 vapor chambers, pore channel with submicron scale provides ultra large vapor–liquid interface area for evaporation heat transfer. Because the pore had ∼100 nm scale and the pore channel had ∼d_m = 556 nm scale, liquid transport in porous media becomes difficult due to the sharply increased flow resistance. In summary, the submicron or nanoscale pore networks formed the obstacle for the two-phase transport, explaining poorer performance of the #3 and #4 vapor chambers.

The four types of deviation degree factors (see Fig. 8) were explained here. The liquid charge ratio was 20%. It should be about 15% for the saturated wetting of the porous media. Thus, about 5% liquid charge ratio was outside of the porous wicks, yielding a liquid layer of about 100 μm thickness on a 90 mm diameter surface. We call such liquid as the extra liquid, whose distribution influences the vapor chamber performance.

Vapor chamber is a capillary force dominated system, explaining the insensitive distribution of $T_{e,c}$ versus inclination angles. This is true for the #1 vapor chamber in the whole heater power range and other vapor chambers at lower heater powers. However, the inclination angle effect occurs at larger heater powers for the #2, #3 and #4 vapor chambers. This is caused by the liquid–vapor phase distribution influenced by various length scales. The Bond number is defined as

$$Bo = \frac{(\rho_l - \rho_g)gL^2}{\sigma} \tag{9}$$

where L is the characteristic length, which is L = Δ = 2.5 mm at θ = 0° (see Fig. 10a). The Bond number is 0.8, indicating both importance of gravity and capillary on the extra liquid distribution. The $Bo \sim 1$ caused the extra liquid settlement of about δ = 100 μm thickness on the particle sub-layer. We remember that the #2 sample with nano-roughness is super-hydrophilic to collect the extra liquid towards the porous stacks. This induces a liquid layer of δ_s within the porous stacks close to the heater wall, yielding an additional thermal resistance corresponding to the liquid layer of δ_s.

Fig. 10b shows the side heating mode at θ = 90°. The Bond number becomes 1100 with L = D, where D is the vapor chamber diameter. The extra liquid settlement is more obvious to from a δ thickness. The heater is located at the vapor chamber center, which is far away from the vapor chamber bottom where δ was marked. Such phase distribution yields a large vapor–liquid interface area for evaporation heat transfer in the vapor chamber center, explaining the lowest $T_{e,c}$, at θ = 90° compared with the other two positions. For the top heating mode (θ = 180°, see Fig. 10c), the extra liquid tends to populate in the tips of the porous stacks, which is away from the heater by a distance of Δ. Because the additional thermal resistance due to liquid layer near the heater wall does not exist, Fig. 10c gives a better thermal performance for the top heating than for the bottom heating. Fig. 10 explains the second type of deviation degree factors for the #2 vapor chamber (see Fig. 8).

For the #3 vapor chamber, Fig. 8 shows the lower temperatures at θ = 90° and 180° than those at θ = 0°. This is because the θ = 90° or 190° positions yield larger vapor–liquid interface area to promote the evaporation heat transfer. Fig. 8 shows the forth type of deviation degree factors. The ε difference between θ = 0° and 180° is not large, but the θ = 90° position had higher temperatures than other positions. Fig. 11 gave the explanation. Fig. 11a shows
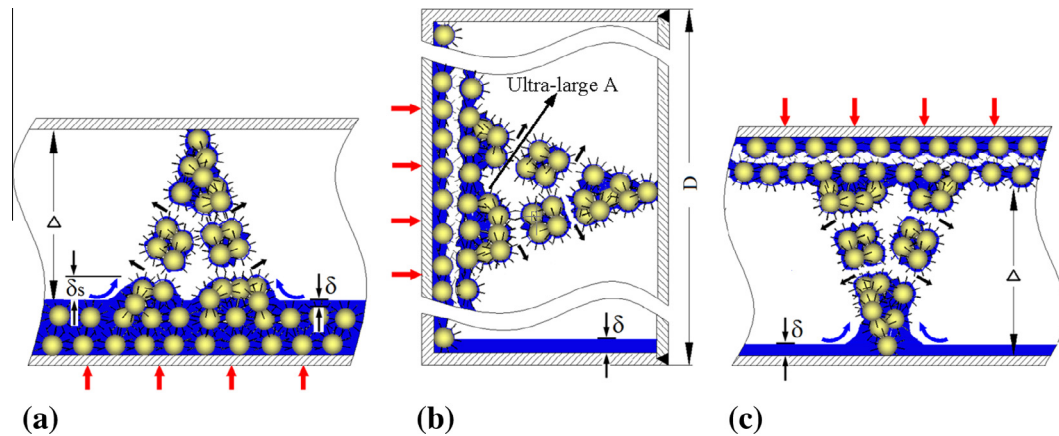
Fig. 10. The second type of wall temperatures with respect to inclination angles (a: bottom heating, b: side heating and c: top heating).
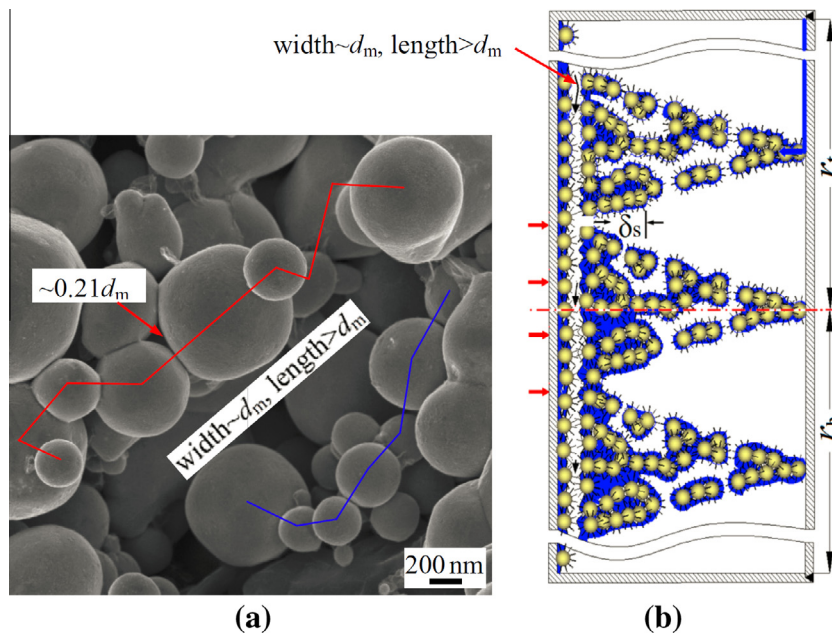

Fig. 11. Nanoscale roughness on submicron particle surfaces (d_m = 556 nm) deteriorates liquid transport to induce the forth type of deviation degree factors (a: pore network, b: phase distribution).

pore network before thermal oxidation, in which pore and pore channel are clearly seen. Fig. 11b shows the side heating operation. The vapor chamber is divided into a top part (r_t) and a bottom part (r_b). The mastoid processes corresponding to the heater location receives liquid from the top part of the vapor chamber, but the liquid in porous stacks is difficult to flow downward due to the increased viscous force in pore channels, reducing the vapor–liquid interface area for the evaporation heat transfer. The nano-roughness on submicron particles further narrowed the pore channel width to increase the flow resistance at the side heating mode, explaining the forth type of deviation degree factors shown in Fig. 8.

It is noted that Figs. 9–11 are the perceptions, which reasonably explained the wall temperature distributions influenced by the gravity force. The flow resistance and phase distribution are strongly related to the liquid charge ratio. In this study, the liquid charge ratio is well maintained to have an ultra thin liquid layer of about 100 μm thickness on the particle surface. Because the material is super-hydrophilic, liquid is preferred to be populated in porous media.

3.4. Boiling curves and heat transfer coefficients

Fig. 12a shows $T_{e,c}$ versus q at $\theta = 180°$. The #1 and #2 vapor chambers had highest and lowest $T_{e,c}$, respectively. The #3 and #4 vapor chambers had $T_{e,c}$ between the #1 and #2 samples. Fig. 12b shows the vapor temperature T_v. Two groups of T_v were observed. No matter at $\theta = 0°$ or 180° and for d_m = 73.8 μm or 556 nm, vapor chambers with nano-roughness significantly decreased vapor temperatures than those with smooth particles. The nano-roughness increased the wettability to enhance the water capture from the condenser surface, yielding ultra thin liquid film on the condenser surface to promote the condensation heat transfer. This explains the lower vapor temperatures with nano-roughness.

Fig. 13 shows boiling curves. The #2 vapor chamber with nano-roughness not only enhances the evaporation heat transfer, but also enlarges the heat flux range, compared with the #1 vapor chamber. The thermal-fluid mechanism is complicated for vapor chambers having submicron particles. The #3 and #4 vapor chambers had intercrossed curves. But the #4 vapor chamber apparently
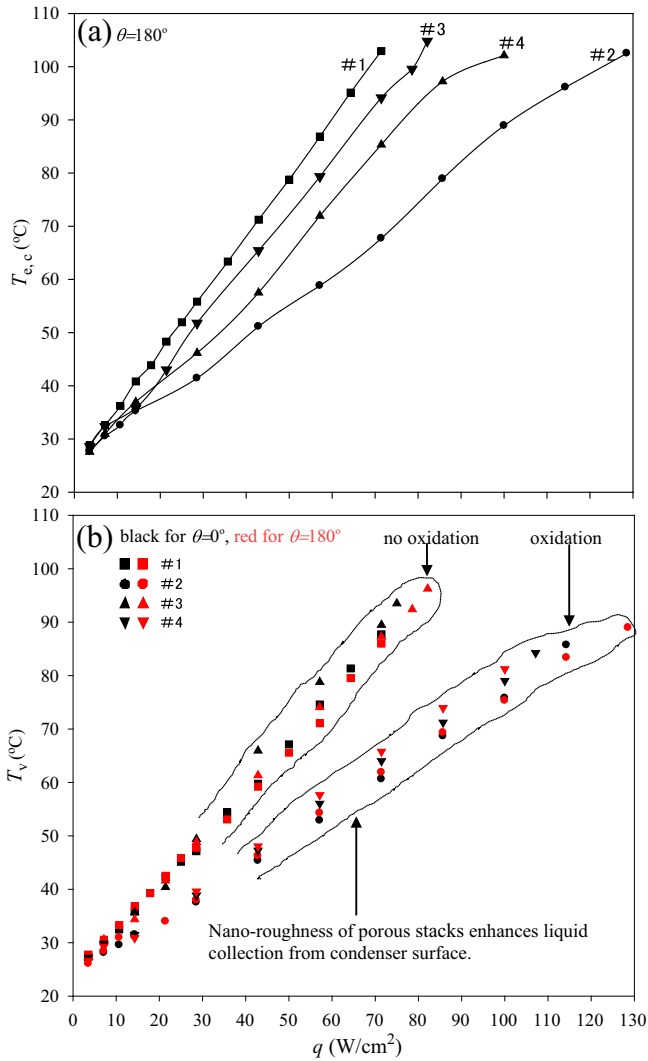
Fig. 12. Evaporator center wall temperatures (a) and inside vapor temperatures (b).

Fig. 13. Boiling curves (a for #1 and #2 vapor chambers, b for #3 and #4 vapor chambers).

extended the heat flux range. The nano-roughness enhances the wettability to prevent the evaporator from dry-out at high heat fluxes.

Fig. 14 shows evaporation and condensation heat transfer coefficients. Nucleate boiling or evaporation heat transfer occurs for evaporators. At low heat fluxes such as $q < 20$ W/cm^2, the evaporator heat transfer coefficients are sharply increased to indicate the nucleate boiling mechanism. At $q > 20$ W/cm^2, heat transfer coefficients are insensitive to the heat fluxes, showing the evaporation heat transfer mechanism.

The #2 vapor chamber had evaporator heat transfer coefficients, h_e, about 3–4 times of those for the #1 vapor chamber, due to the significantly enlarged vapor–liquid interface area with nano-roughness. The #2 vapor chamber had maximum h_e of 120 kW/ m^2 K, but the #1 vapor chamber had h_e of about 35 kW/m^2 K. The #2 vapor chamber decreased h_e at $q > 80$ W/cm^2. Even though $T_{e,c}$ still maintains normal value, the fluid transport in microstructures becomes difficult at high heat fluxes. The evaporator heat transfer coefficients are intercrossed for the #3 and #4 vapor chambers, reflecting the comprehensive influence of micro/nano structures and inclination angles.

Fig. 14b and d show condensation heat transfer coefficients of h_c. The oxidation of mastoid processes promoted h_c to about 14 kW/m^2 K, which is ~18 times of that with smooth particle
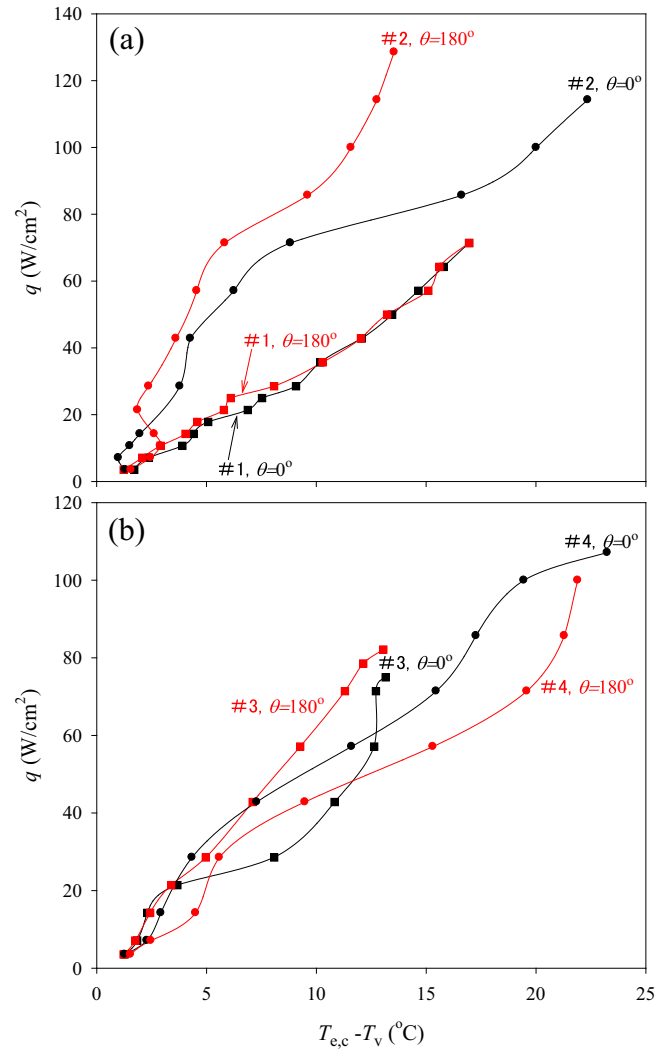
surface. Condensation heat transfer is dependent on the wettability of mastoid processes, not dependent on the pore or pore channel sizes. Fig. 15 plots thermal resistances. For $d_m = 73.8$ μm sintering, the nano-roughness reduces the evaporator thermal resistances to about 1/3–1/2 of those with smooth particle surfaces (see Fig. 15a). The nano-roughness reduces the condenser thermal resistance to about 1/18 of those without nanostructures (see Fig. 15b and d).

3.5. Effect of nanoscale roughness on surface area and wettability

The wettability of solid surface can be changed by varying surface free energy or surface microstructure. The following equation exists [40]:

$$\cos \alpha = \frac{\sigma_{gs} - \sigma_{ls}}{\sigma_{gl}} \qquad (10)$$

where α is the contact angle between liquid and solid surface, the subscripts g, l and s represent gas, liquid and solid, respectively, σ is the surface tension force. If a liquid wets the surface, $\sigma_{gs} - \sigma_{ls}$ is larger than 0. The high energy surface is called for higher surface tension force between gas and solid, such as $\sigma_{gs} > 500$–5000 mN/m. Clean copper, aluminum, zinc surfaces are hydrophilic. Copper oxide (CuO) surface is super-hydrophilic to have a contact angle of about 30° [41,42]. The contact of CuO and H_2O forms hydrogen
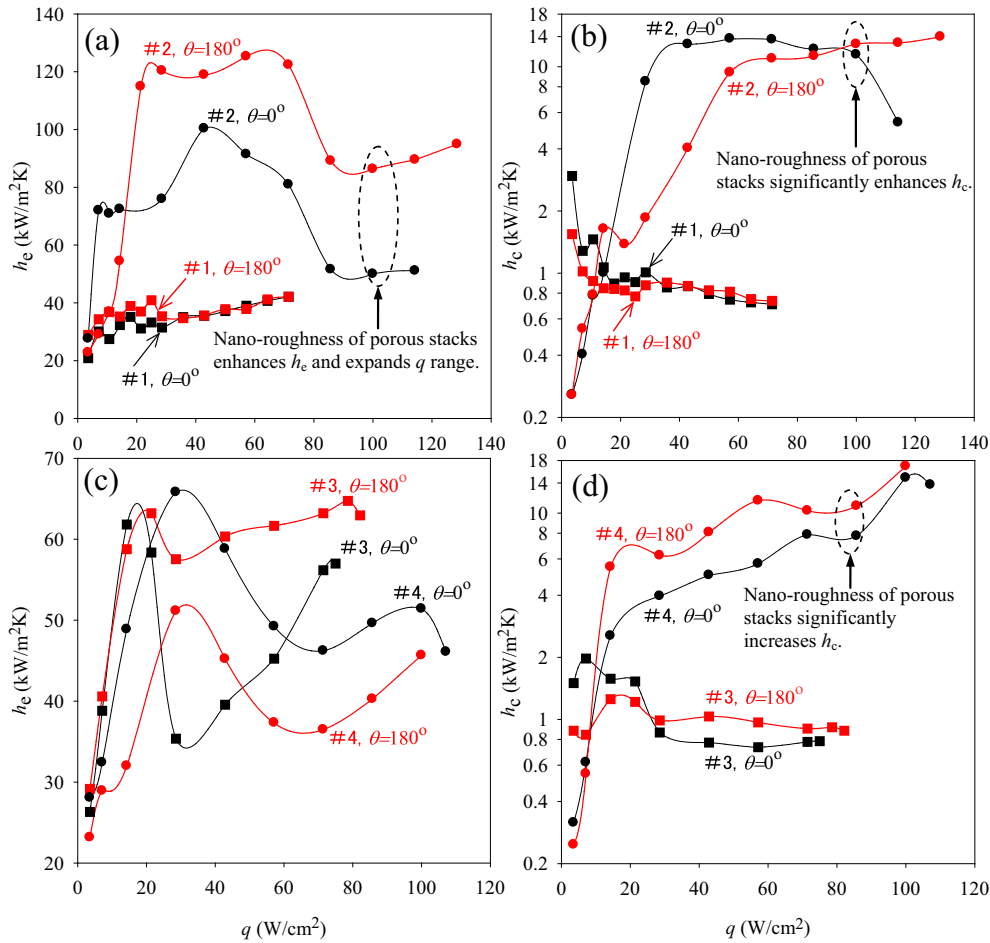
Fig. 14. Evaporator and condenser heat transfer coefficients (a: h_e for #1 and #2, b: h_c for #1 and #2, c: h_e for #3 and #4, d: h_c for #3 and #4).

bond with oxygen atom in CuO and hydrogen atom in H_2O, and coordinate bond with cupric ion and oxygen atom in H_2O. Thus, the concentration of polar molecules is increased to increase the surface wettability.

For a hydrophilic surface, the surface wettability is enhanced by raising the surface roughness. The Wenzel model [43] yields

$$\cos \alpha_w = r \cos \alpha \qquad (11)$$

where α_w is the contact angle between liquid and microstructure surface. We must recognize a distinction between "actual surface" of an interface and what might be called its "geometric surface". The latter is the surface as measured in the plane of the interface. Where perfect smoothness is an acceptable assumption, as at liquid–liquid or liquid–gas interfaces, actual surface and geometric surface are identical, but at the surface of any real solid the actual surface will be greater than the geometric surface because of surface roughness. This surface ratio is termed the "roughness factor" and designated by r:

$$r = \frac{\text{actual surface}}{\text{geometric surface}} \qquad (12)$$

For a flat solid surface, the nanowires had a diameter of a and a height of H. The minimum distance between two neighboring nanowires is b. The roughness factor is

$$r = 1 + \frac{\pi a H}{(a+b)^2} \qquad (13)$$

By introducing two non-dimensional parameters of $\beta = b/a$ and $\xi = H/a$, Eq. (13) becomes

$$r = 1 + \frac{\pi \xi}{(1+\beta)^2} \qquad (14)$$

The Wenzel model (Eq. (11)) told us that the contact angle on nanostructure surface is dependent on r. A copper plate is hydrophilic. When β is fixed, the increase of ξ makes the hydrophilic surface to be more hydrophilic. When nanowires are generated at the solid plate, the surface becomes more hydrophilic due to large ξ. An example was given here for $\beta = 2$ and $\xi = 2.5$, the roughness factor r is 1.8722. The contact angle will be decreased from 60° to 20.5° by Eq. (11).

Now we consider the nanostructures on sphere particles. The particle had a diameter of d. Nanowires had the same dimensions as those on flat solid surface. The roughness factor r becomes

$$r = 1 + \frac{\pi a H}{d^2 \arcsin^2[(a+b)/d]} \qquad (15)$$

Equation (15) reflects the particle size effect on r. For specific a, b and H, the effect of d on r is weak. Thus, the wettability performance is less affected. For $a = 10$ nm, $b = 20$ nm and $H = 25$ nm, the particle $d = 73.8$ μm yields $r = 1.8722$. Alternatively, $d = 556$ nm yields $r = 1.8714$. This estimation explains the similar condensation heat transfer coefficients for the #2 and #4 vapor chambers because the porous stacks had similar water capture capability. In summary, nano-roughness increases the actual surface area to raise the vapor–liquid interface area for evaporation heat transfer enhancement. Another benefit is to increase the wettability to prevent the evaporator from dry-out and enhance the liquid collection capability from the condenser surface.
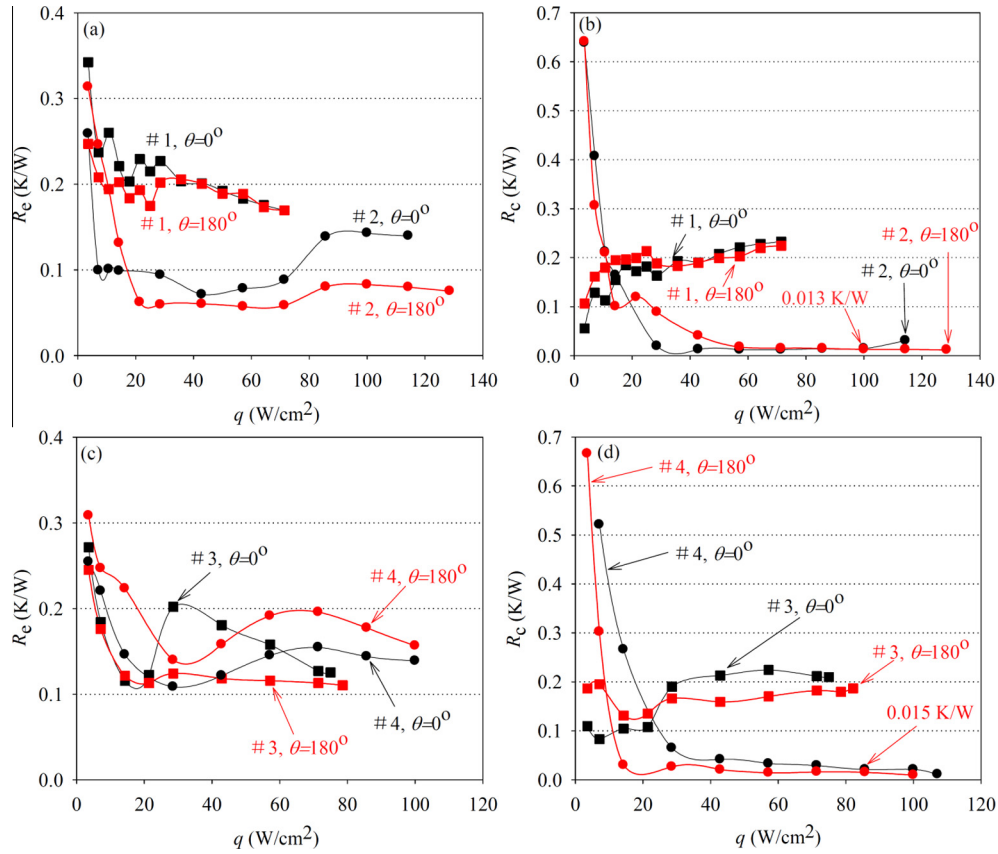
Fig. 15. Evaporator and condenser thermal resistances (a and b for #1 and #2 vapor chambers, c and d for #3 and #4 vapor chambers).

Table 2
Comments on various functions dependent on length scales.

Vapor chambers	Multiscales	Capillary pressure	Liquid transport	Vapor venting	Evaporation heat transfer coefficient	Liquid return from condenser	Condensation heat transfer coefficient
#1	Pore $\sim$0.21d_m; pore channel $\sim d_m$; vapor volume $\sim$mm, where d_m = 73.8 μm	Normal	Good	Good	Not large due to smooth particle surface	Poor due to normal wettability	Not large due to normal liquid collection by porous wick
#2	Nano-roughness (10$\sim$100 nm); pore $\sim$0.21d_m; pore channel $\sim d_m$; vapor volume $\sim$mm, where d_m = 73.8 μm	Super-large due to nanoscale roughness	Good	Good	Perfect due to sufficiently large capillary pressure and extended surface area	Perfect due to the strong wettability of porous stacks	Perfect due to the strong liquid suction by porous stacks
#3	Pore $\sim$0.21d_m; pore channel $\sim d_m$; vapor volume $\sim$mm, where d_m = 556 nm	Good	Normal	Normal	Not large due to pore channel blocking effect	Normal due to normal wettability without nano-roughness	not Large due to normal liquid collection by porous wick
#4	Nano-roughness (10$\sim$100 nm); pore $\sim$0.21d_m; pore channel $\sim d_m$; vapor volume $\sim$mm, where d_m = 556 nm	Super-large due to nanoscale roughness	Poor due to the strong pore channel blocking effect	Poor due to the strong pore channel blocking effect	Not large due to pore channel blocking effect	Perfect due to the strong wettability of porous stacks	Perfect due to the strong liquid suction by porous stacks

3.6. The synergy consideration of the four vapor chambers

The vapor chambers had fruitful multiscales. We identified if these length scales are matched with each other to improve the heat pipe performance. Table 2 summaries length scales, capillary pressures, liquid transport, vapor venting, evaporation heat transfer, liquid return from condenser and condensation heat transfer. Comments are given for these functions corresponding to specific length scales.

The #1 vapor chamber had the poorest performance. Even though fluid transport is smooth going with $\sim d_m$ = 73.8 μm pore channel, the evaporation heat transfer is not good without nanoscale involved. The condensation heat transfer coefficients are low, due to the normal wettability of mastoid process array.

The #2 vapor chamber had four length scales. The $\sim$mm scale outside of mastoid processes are for the vapor population. The pore channels with d_m = 73.8 μm scale smoothly transport fluid in porous media. The nano-roughness increased surface area to enhance

the evaporation heat transfer. The increased wettability of porous stacks enhances the liquid collection from the condenser to enhance the condensation heat transfer. *The four length scales are adapted with each to successfully overcome various conflicts for heat pipes.*

The #3 and #4 vapor chambers showed poor overall performance. For the #4 vapor chamber, the nano-roughness creates large capillary pressures and expands surface area. The increased wettability increases the liquid collection from the condenser to maintain high condensation heat transfer coefficients. But further narrowed pore channels hinder the fluid transport to deteriorate the evaporation heat transfer. *The submicron particle sintering and the nano-roughness are the poor match, which cannot coordinate conflicts for heat pipes.*

The decoupling and synergy strategy guides the multiscale construction. The device can work at different inclination angles on earth. The side and top heating modes even have better performance than the bottom heating mode, if liquid in the porous stacks at the heater region can be freely transported to elsewhere. It is expected the multiscale heat pipes can work under varied gravity levels such as on board a space ship.

4. Conclusions

The conclusions are summarized as follows:

- The decoupling and synergy strategy was proposed to construct multiscales for heat pipes. The first step decouples a heat pipe into a set of functions and assigns suitable length scale to activate specific functions. The second step verifies the synergy of various length scales to adapt functions.
- Four vapor chambers were fabricated by sintering d_m = 73.8 μm or d_m = 556 nm particles, with and without thermal oxidation on particle surfaces. The SEM images show multiscale behavior and the water suction tests show the hydrophilic mastoid process.
- The #2 vapor chamber had the best performance, due to the match of each length scale with corresponding function. The #3 and #4 vapor chambers had poor performance, due to the narrowed pore channels to transport fluids.
- Four types of deviation degree factors were found. The difference between the bottom and top heating modes is not large. The side heating mode had apparently different temperatures. For the side heating, the #2 vapor chamber had lower temperatures, due to the free moving of liquids from the heater region to the bottom region. The #4 vapor chamber had high temperatures, due to the liquid blockage effect in pore channels.
- The #2 vapor chamber with nano-roughness not only had large evaporation heat transfer coefficients, but also enlarged the heat flux range. The #4 vapor chamber with nano-roughness increased the hydrophilic degree to extend the heat flux range, but the evaporation heat transfer coefficients were low.
- Nano-roughness of mastoid processes increased the wettability to enhance the water capture from the condenser. The condensation heat transfer coefficients can be increased by 18 times using the evaporator wettability enhancement.
- The ∼100 μm particle sintering and the nanostructure are the best combination to coordinate various conflicts, but the submicron particle sintering and the nanostructure are the poor match, which cannot coordinate conflicts for heat pipes.

Acknowledgements

References

[1] L.L. Vasiliev, Micro and miniature heat pipes-electronic component coolers, Appl. Therm. Eng. 28 (2008) 266–273.

[2] F.L. Chang, Y.M. Hung, The coupled effects of working fluid and solid wall on thermal performance of micro heat pipes, Int. J. Heat Mass Transfer 73 (2014) 76–87.

[3] Y. Maydanik, Loop heat pipes, Appl. Therm. Eng. 25 (2005) 635–657.

[4] C. Petit, B. Siedel, D. Gloriod, V. Sartre, F. Lefevre, J. Bonjour, Adsorption-based antifreeze system for loop heat pipes, Appl. Therm. Eng. 78 (2015) 704–711.

[5] J.L. Xu, Y.X. Li, T.N. Wong, High speed flow visualization of a closed loop pulsating heat pipe, Int. J. Heat Mass Transfer 48 (2005) 3338–3351.

[6] M. Gonzalez, B. Kelly, Y. Hayashi, Y.J. Kim, Heat transfer mechanisms in pulsating heat-pipes with nanofluid, Appl. Phys. Lett. 106 (2015) 013906, http://dx.doi.org/10.1063/1.4905554.

[7] M.C. Tsai, S.W. Kang, K.V. de Paiva, Experimental studies of thermal resistance in a vapor chamber heat spreader, Appl. Therm. Eng. 56 (2013) 38–44.

[8] S.C. Wong, S.F. Huang, K.C. Hsieh, Performance tests on a novel vapor chamber, Appl. Therm. Eng. 31 (2011) 1757–1762.

[9] V. Ayel, L. Araneo, A. Scalambra, M. Mameli, C. Romestant, A. Piteau, M. Marengo, S. Filippeschi, Y. Bertin, Experimental study of a closed loop flat plate pulsating heat pipe under a varying gravity force, Int. J. Therm. Sci. 96 (2015) 23–34.

[10] D.C. Mo, N. Ding, S.S. Lu, Gravity effects on the performance of a flat loop heat pipe, Microgravity Sci. Technol. 21 (Suppl. 1) (2009) S95–S102.

[11] W. Deng, Z. Xie, Y. Tang, R. Zhou, Experimental investigation on anti-gravity loop heat pipe based on bubbling mode, Exp. Therm. Fluid Sci. 41 (2012) 4–11.

[12] R.S. Dietz, The meteoritic impact origin of the Moon's surface features, J. Geol. 54 (6) (1946) 359–375.

[13] K.V. Paiva, M.B.H. Mantelli, L.K. Slongo, Experimental testing of mini heat pipes under microgravity conditions aboard a suborbital rocket, Aerosp. Sci. Technol. 45 (2015) 367–375.

[14] X.M. Yang, Z.W. Zhong, E.Q. Li, Z.H. Wang, W. Xu, S.T. Thoroddsen, X.X. Zhang, Asymmetric liquid wetting and spreading on surfaces with slanted micro-pillar arrays, Soft Matter 9 (2013) 11113–11119.

[15] Y. Nam, Y.S. Ju, A comparative study of the morphology and wetting characteristics of micro/nanostructured Cu surfaces for phase change heat transfer applications, J. Adhes. Sci. Technol. 27 (2013) 2163–2176.

[16] M.M. Zogbi, J.E. Saito, H. Zanin, F.R. Marciano, A.O. Lobo, Hydrothermal–electrochemical synthesis of nano-hydroxyapatite crystals on superhydrophilic vertically aligned carbon nanotubes, Mater. Lett. 132 (2014) 70–74.

[17] C.H. Li, T. Li, P. Hodgins, C.N. Hunter, A.A. Voevodin, J.G. Jones, G.P. Peterson, Comparison study of liquid replenishing impacts on critical heat flux and heat transfer coefficient of nucleate pool boiling on multiscale modulated porous structures, Int. J. Heat Mass Transfer 54 (2011) 3146–3155.

[18] C. Byon, S. Choi, S.J. Kim, Critical heat flux of bi-porous sintered copper coatings in FC-72, Int. J. Heat Mass Transfer 65 (2013) 655–661.

[19] C. Byon, S.J. Kim, Capillary performance of bi-porous sintered metal wicks, Int. J. Heat Mass Transfer 55 (2012) 4096–4103.

[20] T. Semenic, Y.Y. Lin, I. Catton, D.B. Sarraf, Use of biporous wicks to remove high heat fluxes, Appl. Therm. Eng. 28 (2008) 278–283.

[21] D.H. Min, G.S. Hwang, Y. Usta, O.N. Cora, M. Koc, M. Kaviany, 2-D and 3-D modulated porous coatings for enhanced pool boiling, Int. J. Heat Mass Transfer 52 (2009) 2607–2613.

[22] G.S. Hwang, M. Kaviany, W.G. Anderson, J. Zuo, Modulated wick heat pipe, Int. J. Heat Mass Transfer 50 (2007) 1420–1434.

[23] C. Byon, S.J. Kim, Capillary performance of bi-porous sintered metal wicks, Int. J. Heat Mass Transfer 55 (2012) 4096–4103.

[24] Z. Liu, H. Li, B. Chen, J. Yang, W. Liu, Operational characteristics of flat type loop heat pipe with biporous wick, Int. J. Therm. Sci. 58 (2012) 180–185.

[25] X.B. Ji, J.L. Xu, Z.W. Zhao, W.L. Yang, Pool boiling heat transfer on uniform and non-uniform porous coating surfaces, Exp. Therm. Fluid Sci. 48 (7) (2013) 198–212.

[26] T. Semenic, I. Catton, Experimental study of biporous wicks for high heat flux applications, Int. J. Heat Mass Transfer 52 (2009) 5113–5121.

[27] D. Ćoso, V. Srinivasan, M.-C. Lu, J.Y. Chang, A. Majumdar, Enhanced heat transfer in biporous wicks in the thin liquid film evaporation and boiling regimes, J. Heat Transfer Trans. ASME 134 (2012). 101501.

[28] A. Zou, S.C. Maroo, Critical height of micro/nano structures for pool boiling heat transfer enhancement, Appl. Phys. Lett. 103 (2013) 221602, http://dx.doi.org/10.1063/1.4833543.

[29] L. Dong, X. Quan, P. Cheng, An experimental investigation of enhanced pool boiling heat transfer from surfaces with micro/nano-structures, Int. J. Heat Mass Transfer 71 (2014) 189–196.

[30] B.S. Sikarwar, S. Khandekar, K. Muralidhar, Simulation of flow and heat transfer in a liquid drop sliding underneath a hydrophobic surface, Int. J. Heat Mass Transfer 57 (2013) 786–811.

[31] D.A. Benson, R.T. Mitchell, M.R. Tuck, D.W. Palmer, G.P. Peterson, Ultra high capacity micro machined heat spreaders, Microscale Therm. Eng. 2 (1998) 21–30.

[32] J.B. Boreyko, C.H. Chen, Vapor chambers with jumping-drop liquid return from superhydrophobic condensers, Int. J. Heat Mass Transfer 61 (2013) 409–418.

[33] K. Koch, W. Barthlott, Superhydrophobic and superhydrophilic plant surfaces: an inspiration for biomimetic materials, Philos. Trans. R. Soc. A 367 (2009) 1487.

[34] B. Bhushan, Biomimetics: lessons from nature-an overview, Philos. Trans. R. Soc. A 367 (2009) 1445.

[35] P.R. Bevington, D.K. Robinson, Data Reduction and Error Analysis for the Physical Sciences, third ed., McGraw-Hill, New York, 2003.

[36] S.W. Chi, Heat Pipe Theory and Practice, Hemisphere, McGraw-Hill, Washington, D.C., New York, 1976.

[37] D. Or, Scaling of capillary, gravity and viscous forces affecting flow morphology in unsaturated porous media, Adv. Water Resour. 31 (2008) 1129–1136.

[38] S. Kirdponpattara, M. Phisalaphong, B.Z. Newby, Applicability of Washburn capillary rise for determining contact angles of powders/porous materials, J. Colloid Interface Sci. 397 (2013) 169–176.

[39] H.X. Chen, J.L. Xu, Z.J. Li, F. Xing, J. Xie, W. Wang, W. Zhang, Flow pattern modulation in a horizontal tube by the passive phase separation concept, Int. J. Multiphase Flow 45 (2012) 12–23.

[40] P.D. Gennes, F. Brochard-Wyard, D. Quere, Capillarity and Wetting Phenomena: Drops, Bubbles, Pearls, Waves, Springer, 2004.

[41] F.M. Chang, S.L. Cheng, S.J. Hong, Y.J. Sheng, H.K. Tsao, Superhydrophilicity to superhydrophobicity transition of CuO nanowire films, Appl. Phys. Lett. 96 (2010) 114101.

[42] Z.G. Guo, W.M. Liu, B.L. Su, A stable lotus-leaf-like water-repellent copper, Appl. Phys. Lett. 92 (2008) 063104.

[43] R.N. Wenzel, Resistance of solid surfaces to wetting by water, J. Ind. Eng. Chem. 28 (1936) 988–994.